Topological defects as relics of emergent continuous symmetry and Higgs condensation of disorder in ferroelectrics

Shi-Zeng Lin[1][†], Xueyun Wang[2][†], Yoshitomo Kamiya[1,3], Gia-Wei Chern[1], Fei Fan[2,4], David Fan[2,5], Brian Casas[2,6], Yue Liu[2,7], Valery Kiryukhin[2], Wojciech H. Zurek[1], Cristian D. Batista[1] and Sang-Wook Cheong[2]*

Lars Onsager and Richard Feynman envisaged that the three-dimensional (3D) superfluid-to-normal λ transition in [4]He occurs through the proliferation of vortices. This process should hold for every phase transition in the same universality class. The role of topological defects in symmetry-breaking phase transitions has become a prime topic in cosmology and high-temperature superconductivity, even though direct imaging of these defects is challenging. Here we show that the U(1) continuous symmetry that emerges at the ferroelectric critical point of multiferroic hexagonal manganites leads to a similar proliferation of vortices. Moreover, the disorder field (vortices) is coupled to an emergent U(1) gauge field, which becomes massive by means of the Higgs mechanism when vortices condense (span the whole system) on heating above the ferroelectric transition temperature. Direct imaging of the vortex network in hexagonal manganites offers unique experimental access to this dual description of the ferroelectric transition, while enabling tests of the Kibble–Zurek mechanism.

Phase transitions are among the most fascinating phenomena of nature. Understanding their mechanisms is one of the foremost challenges of modern physics. In a nutshell, the goal is to understand how the 'generalized rigidity' of the ordered phase emerges through a spontaneous symmetry breaking on cooling across the critical temperature T_c (ref. 1). An attractive aspect of these transitions is the universal behaviour that makes them independent of microscopic details. The universality class is determined by a few fundamental properties, including symmetry, range of interactions, dimensionality and number of components of the order parameter. In addition, the Wilson–Fisher[2] paradigm gave birth to another deep concept known as emergent symmetry. The basic idea is that the effective action that describes the long-wavelength fluctuations near the critical point may have more symmetries than the original microscopic action. This notion implies that systems such as magnets or ferroelectrics, which only possess discrete symmetries at a microscopic level, may have an emergent continuous symmetry at a critical point, as was demonstrated by Jose, Kadanoff, Kirkpatrick and Nelson in their seminal work[3].

As envisaged by Onsager and Feynman[4,5], the restoration of a continuous U(1) symmetry, such as the superfluid to normal transition of [4]He, can occur by the proliferation of vortices. The role of these topological defects in symmetry-breaking phase transitions is now a prime topic in different areas of physics, such as cosmology[6,7] and high-T_c superconductivity[8–12], even though

they are difficult to observe[13]. The potential of having emergent continuous symmetries in magnets or ferroelectrics with discrete microscopic symmetries opens the possibility of observing a similar proliferation of vortices in insulating materials. Although the emergence of continuous symmetries from discrete variables is theoretically established, the same is not true at the experimental level. Among other reasons, it is always challenging to measure critical exponents with the required resolution to distinguish between discrete and continuous symmetry breaking. Here we demonstrate the emergence of a continuous U(1) symmetry at the ferroelectric transition of the hexagonal manganites $RMnO_3$ (R = Y, Ho, … Lu, Sc) by directly measuring the vortices or disorder field, instead of addressing the order parameter field. An emergent U(1) symmetry implies that the critical point belongs to the XY universality class, which is the class of the superfluid transition of a neutral system such as [4]He. Therefore, analogous with the case of superfluid [4]He, the transition must be driven by a proliferation of vortices spanning the whole system above T_c. In this dual description, based on the disorder field of topological vortices instead of the order parameter field[14–16] (Box 1), the phase transition is described as a condensation of a disorder field which is coupled to a gauge field[10,14]. On heating across T_c, the vortex condensation makes the gauge field massive via the Higgs mechanism. Consequently, the vortex–vortex interaction becomes screened above T_c, instead of the Biot–Savart interaction that characterizes the Coulomb phase below T_c. Figure 1a,b shows

[1]Theoretical Division, T-4 and CNLS, Los Alamos National Laboratory, Los Alamos, New Mexico 87545, USA. [2]Rutgers Centre for Emergent Materials and Department of Physics and Astronomy, Rutgers University, 136 Frelinghuysen Road, Piscataway, New Jersey 08854, USA. [3]iTHES Research Group and Condensed Matter Theory Laboratory, RIKEN, Wako, Saitama 351-0198, Japan. [4]Shaanxi Key Laboratory of Condensed Matter Structures and Properties, School of Science, Northwestern Polytechnical University, Xi'an 710129, China. [5]Montgomery High School, 1016 Route 601, Skillman, New Jersey 08558, USA. [6]Functional Materials Laboratory, Department of Physics, University of South Florida, Tampa, Florida 33613, USA. [7]The MOE key Laboratory of Weak-Light Nonlinear Photonics and TEDA Applied Physics School, Nankai University, Tianjin 300457, China. [†]These authors contributed equally to this work. *e-mail: sangc@physics.rutgers.edu
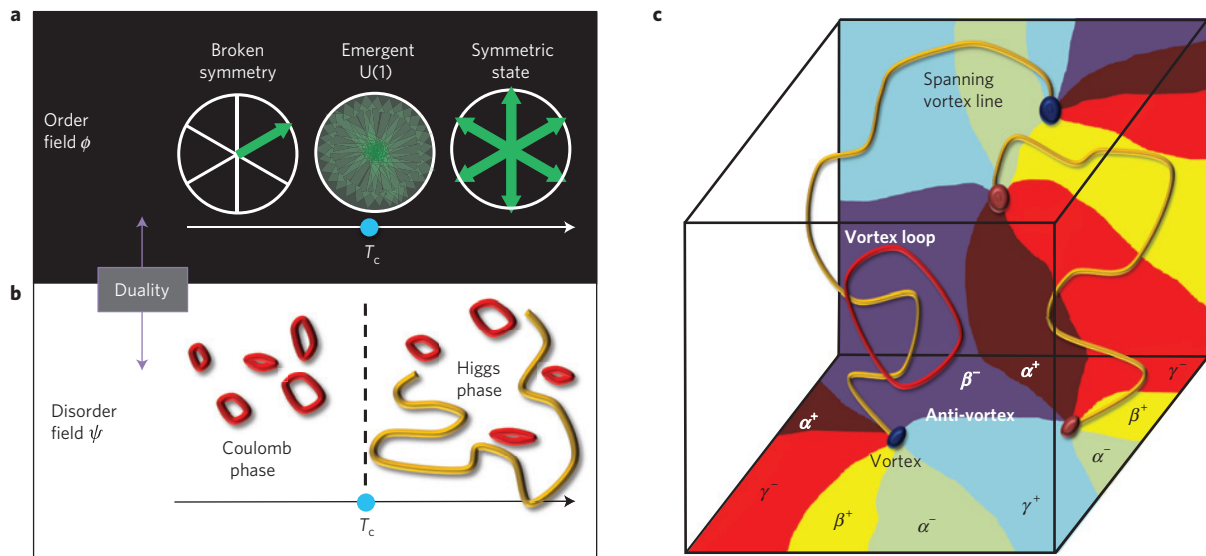
Figure 1 | Dual description of a phase transition with Z₂ × Z₃ symmetry. The phase transition can be described in terms of the order field ϕ (**a**) or the disorder field ψ (**b**). The local order parameter ϕ takes six values, represented by the even hours in the clock dials in **a**. They correspond to the six multiferroic states or domains α^+ through γ^- distinguished by the polarization direction (+ or −) and the trimerization phase (α, β, γ), as described in the text. The multiferroic $Z_2 \times Z_3$ vortices are line defects where the six domains meet with each other, as shown in **c**. Continuous U(1) symmetry emerges from $Z_2 \times Z_3$ order parameter at the critical temperature. The disordered phase above T_c can be described as a condensation of the disorder field ψ signalled by the proliferation of vortex lines spanning the whole system (yellow lines). Only quickly fluctuating closed vortex loops (red lines) are present for $T < T_c$. The Higgs and Coulomb phases of the disorder field are described in Box 1.

Box 1 | Duality.

The local order parameter of our problem is a complex field $\phi_j = |\phi_j| e^{i\varphi_j}$, that takes six possible values ($Z_2 \times Z_3$) corresponding to the even times of a clock. By assuming that the local trimerization and dipole moments develop above T_c, we neglect the amplitude ($|\phi_j|$) fluctuations near T_c. The six orientations of ϕ_j are enforced by an effective potential, $V(\phi_j) = A \cos(6\varphi_j)$, which reflects the anisotropy of the underlying crystal lattice. $V(\phi_j)$ is dangerously irrelevant at T_c—that is, the coarse-grained action near the ferroelectric transition becomes identical to the isotropic ϕ^4 action for the normal to superfluid transition of a neutral system such as ^{4}He (Fig. 1a):

$$H_\phi = m_\phi^2 \phi^2 + u_\phi \phi^4 + (\nabla\phi)^2 \qquad (2)$$

where m_ϕ and u_ϕ are the mass and coefficient of the quartic term for the field ϕ. The superfluid to normal transition occurs by the proliferation of vortex lines at $T > T_c$. The problem admits a dual description, in which the proliferation of vortex lines spanning the whole system arises from a condensation of a dual or 'disorder' field $\psi = |\psi| e^{i\theta}$ minimally coupled to an effective gauge field. Below T_c, the 'photon' of this gauge field is the Goldstone mode of the superfluid field ϕ. This photon acquires a finite mass via the Higgs mechanism for $T > T_c$

(Fig. 1b). Consequently, the Biot–Savart (Coulomb) interaction between vortex segments for $T < T_c$ becomes screened (Yukawa) for $T > T_c$.

The dual description is obtained after a sequence of transformations. The original ϕ^4 theory (2) for a neutral superfluid is first mapped into a loop gas of vortices coupled to a vector gauge field **A** generated by the smooth phase fluctuations of the original field ϕ. The fluctuating vortex loops are then described by a disorder $|\psi|^4$ field theory in which the vortex loops correspond to 'supercurrents' of ψ, which remain minimally coupled to **A** (refs 14–16):

$$H_\psi = m_\psi^2 \psi^2 + u_\psi \psi^4 + \frac{1}{2t}|(\nabla - iq_{\text{eff}}\mathbf{A})\psi|^2 + \frac{1}{2}(\nabla \times \mathbf{A})^2$$

where m_ψ and u_ψ are the mass and coefficient of the quartic term for the disorder field ψ. The constants t and q_{eff} are determined by non-universal parameters, such as the vortex core energy and the transition temperature[14–16]. Having direct experimental access to the vortex field, we can observe the Higgs condensation of ψ: the emergence of vortex lines that span the whole system above T_c implies that superfluid currents of the disorder field ψ connect opposite ends of the sample—that is, the disorder field has condensed into a 'superfluid state' (Fig. 1b).

---

the same phase diagram from two different viewpoints with the order and disorder fields. We will see below that the possibility of freezing vortices in the hexagonal RMnO₃ provides a unique opportunity to experimentally access both the dual theory and the Higgs condensation of disorder in insulating materials.

The dynamics of symmetry breaking in phase transitions is another fascinating phenomenon that can be tested in

RMnO₃. Its salient features are captured by the Kibble–Zurek mechanism (KZM), which combines cosmological motivations with information about the near-critical behaviour. Symmetry breaking is thought to be responsible for the emergence of the familiar fundamental interactions from the unified field theory at Grand Unification Theory temperatures of $\sim 10^{15}$ GeV in the cooling of the Universe after the Big Bang. As Kibble[17] noted,
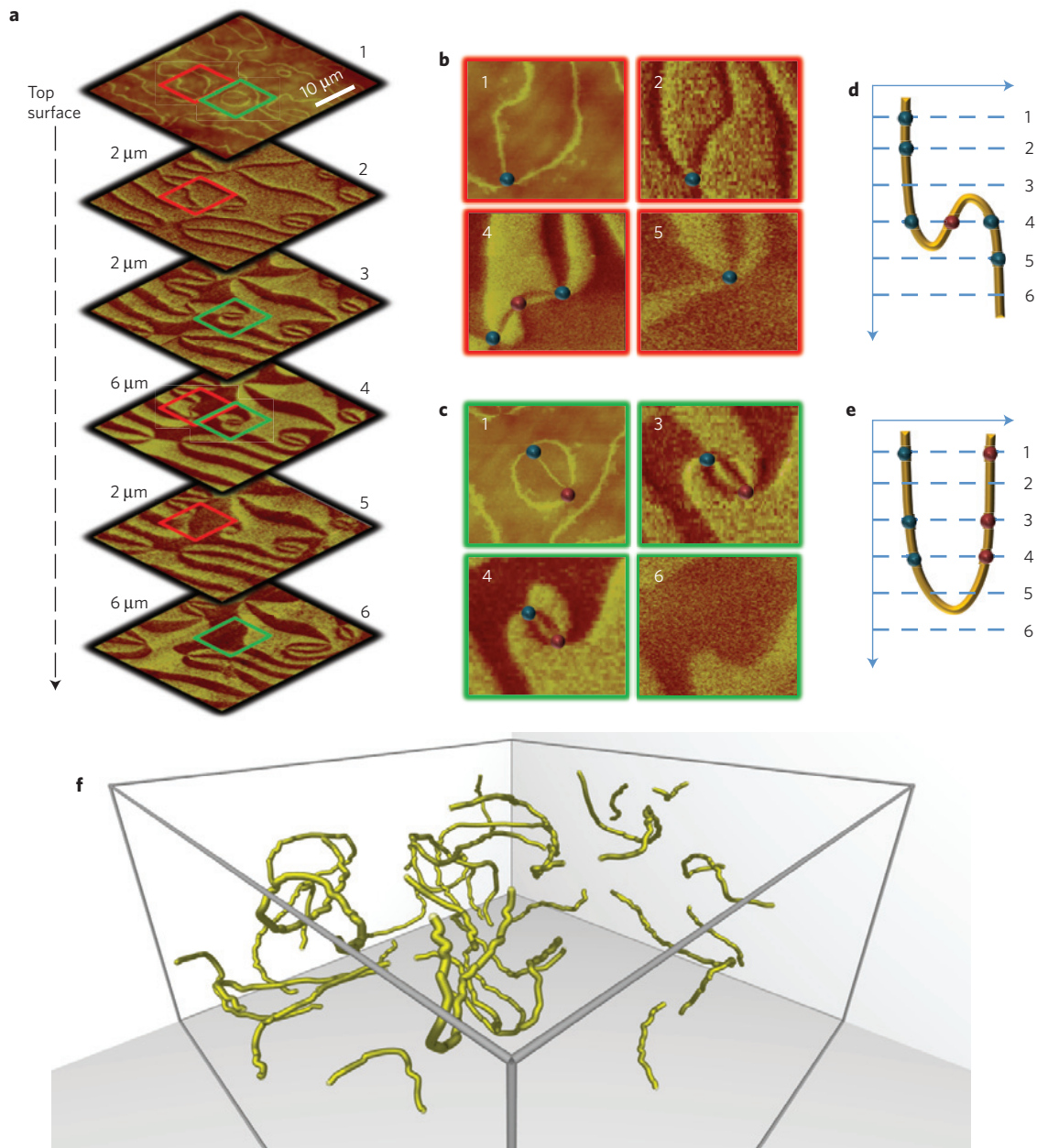
Figure 2 | 3D picture of vortex cores: depth profiling of vortex domain patterns. a, Evolution of the $Z_2 \times Z_3$ ferroelectric domains on the polished surface of a hexagonal-$LuMnO_3$ crystal, which was consecutively thinned down. The depth of each polished surface from the original surface is shown in micrometres. Layer 1 is an atomic force microscope image on the unpolished, but chemically etched surface. Layers 2–6 are PFM images on the same area with different depths. The dark and light regions correspond to the domains with opposite electric polarizations. **b,c**, Enlarged areas exhibiting the evolution of the vortex and antivortex cores (labelled as blue and red dots, respectively) in the red-boxed and green-boxed regions of **a**. Vortex–antivortex pairs can be observed. The structural phases forming such pairs are identified in Fig. 3b. **d,e**, The obtained depth profiles of the vortex cores for the regions shown in **b,c**, respectively. **f**, Vortex loops and lines spanning the whole system obtained from our Monte Carlo simulations of the 3D clock model of equation (1) at $T > T_c$.

relativistic causality limits the size of domains that can coordinate the choice of broken symmetry in the nascent Universe. This results in a random selection of local broken symmetry, and can lead to the creation of topological defects (for example, monopoles or cosmic strings) that influence the evolution of the Universe.

Because phase transitions are ubiquitous, their dynamics can be investigated experimentally. Although relativistic causality is no longer a useful constraint in the laboratory, cosmological motivations can be combined with the scaling relations in the

near-critical regime of second-order phase transitions to estimate the density of topological defects as a function of the quench rate[18]. This combination defines the Kibble–Zurek mechanism[7,19].

Topological defects are not only clearly visible in $RMnO_3$, but (in contrast to, for example, superfluids) they are immobilized by the structure of the material, which solidifies below the critical point. Consequently, they can be seen and counted at leisure, long after the transition. Moreover, in contrast to other systems used as a test bed for KZM (refs 20–27), the quench timescale τ_Q can be varied over orders of magnitude. This is important, as

densities of defects predicted by KZM often scale as τ_Q to a small fractional power.

Model

The onset of ferroelectricity in RMnO$_3$ (T_c values of YMnO$_3$, ErMnO$_3$, TmMnO$_3$, LuMnO$_3$ are $\approx$1,250, 1,403, 1,523, 1,672 K, respectively) is triggered by a structural instability called trimerization and a subsequent ionic displacement with a net electric dipole moment. Whereas trimerization breaks the Z$_3$ symmetry of the hexagonal lattice, the subsequent distortion breaks an additional Z$_2$ symmetry (sign of the electric polarization along the c axis, perpendicular to the hexagonal plane)[28–33]. (Note that Z$_6$ does not refer to the homotopy group in this context, but to the fact that these vortices are made of six domains.) The transition then breaks a Z$_3 \times$ Z$_2$ symmetry group and it is described by an effective $p = 6$ clock model,

$$H = J \sum_{\langle j,l \rangle} \cos(\varphi_j - \varphi_l) + J' \sum_{\langle j,l \rangle} \cos(\varphi_j - \varphi_l) \qquad (1)$$

known to exhibit an emergent U(1) symmetry at the critical point[3]. The phase $\varphi_j = n\pi/3$ takes six possible values when the integer n runs between 0 and 5. The six minima of this Hamiltonian can be labelled by the even hours on the clock face, which justifies the name of the model. The electric polarization P$_j \propto \cos(3\varphi_j)$ is perpendicular to the triangular layers. The trimerization parameter is described by a 2D vector $\mathbf{T}_j \propto (\cos(2\varphi_j), \sin(2\varphi_j))$ with three possible orientations, which will be denoted by (α, β, γ). J and J' are effective coupling constants between nearest-neighbour variables j and l on the same triangular layer and on adjacent layers, respectively. Because the six-fold anisotropy becomes relevant away from the critical point, the usual U(1) vortices of the XY model are replaced by the Z$_6$ vortices that are observed in the experiments[28–33]. The formation of these six-state vortices, shown in Fig. 1c, originates from the cyclic arrangement of six interlocked structural antiphase (α, β, γ) and ferroelectric $(+/-)$ ground states. According to equation (1), there are only two low-energy cyclic arrangements, which correspond to the vortex $(\alpha^+, \beta^-, \gamma^+, \alpha^-, \beta^+, \gamma^-)$ and the anti-vortex $(\alpha^+, \gamma^-, \beta^+, \alpha^-, \gamma^+, \beta^-)$, in agreement with the experimental observations[28–33], see Fig. 1c. Any other cyclic arrangement contains domain walls with higher energy $(|\Delta\varphi| > \pi/3)$.

As we explained above, the six-fold anisotropy of the clock model is dangerously irrelevant[34,35]—that is, the critical point belongs to the XY universality class but the discreteness becomes relevant away from T_c. Because the critical region around T_c can be described by the same Ginzburg–Landau ϕ^4 theory that describes the transition of a neutral superfluid (Box 1), the ferroelectric order parameter is also destroyed by proliferation of (Z$_6$) vortices. According to the dual theory (see Fig. 1 and Box 1), a finite fraction of vortex lines span the whole system above T_c—that is, the corresponding vortex cores connect opposite surfaces of the sample. Therefore, it is natural to conjecture that the six-state vortex domain structures observed on the surface of RMnO$_3$ correspond to transverse cuts of these vortex cores. This conjecture is substantiated by the piezoresponse force microscope (PFM) 3D images of vortex cores in the hexagonal-LuMnO$_3$ crystal (See Supplementary Section 1 for the method). These images are obtained after a sequence of three steps: heating a hexagonal LuMnO$_3$ single crystal up to $T = 1,723$ K ($> T_c \approx 1,672$ K); keeping the temperature constant for 30 min; and cooling the specimen down to room temperature. The emergence of a vortex domain pattern on the a–b surface of the crystal is revealed by chemical etching. To obtain a 3D picture of vortex cores (that is, a depth profiling of vortex domain patterns), the sample is polished along the c axis and PFM images of the same region are taken for different depths (Fig. 2a). Enlarged areas exhibiting the
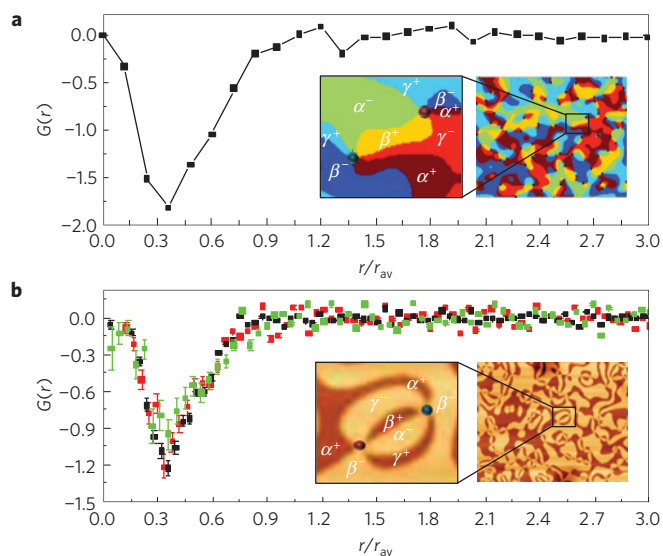
Figure 3 | Vortex–antivortex pair correlation function. a, Theoretical vortex–antivortex pair correlation function $G(r)$ for the configuration obtained on the surface of the system after annealing from $T_i = 6.0 J$ to $T_f = 0.0 J$ at a rate $\Delta T = 0.001 J$ per MC sweep. **b**, Measured $G(r)$ for three different samples with different vortex densities: ErMnO$_3$ (green), YMnO$_3$ (black) and YbMnO$_3$ (red). The distances are scaled by the average defect separation r_{av}, making the shown quantities dimensionless. Error bars are from counting statistics and represent one standard deviation. The insets show parts of the domain patterns obtained in the calculations (**a**) and experimentally measured by AFM in YbMnO$_3$ (**b**). The magnified images show vortex–antivortex pairs in small regions of these patterns, with the structural phases labelled.

depth evolution of vortex cores in the red and green boxed regions are shown in Fig. 2b,c, respectively. The large spatial extension of vortex cores is evident in the figure. The schematics of the vortex networks shown in Fig. 2d,e are obtained by depth profiling of the 2D vortex cores.

To simulate this phenomenon, we ran Monte Carlo (MC) simulations of equation (1) based on a local update Metropolis algorithm because the microscopic dynamics of RMnO$_3$ is expected to be local (see Supplementary Section 2 for the simulation details). The lattice size is $L^2 \times L_z$ with $L = 192 a$ and $L_z = 96 a$ (a is the lattice parameter). We used periodic boundary conditions in the xy plane and open boundary conditions along the z direction. The critical temperature obtained for $J' = J$ is $T_c \approx 3.03J$. The vortices shown in Fig. 2f were obtained after annealing from an initial temperature $T_i = 6.0J$ down to $T_f = 0$ at a rate $\Delta T = 0.005J$ per MC sweep (MCS). To verify that they reproduce the experimental observation (Fig. 2a), we compared the distributions of pointlike vortices and anti-vortices on a given layer (see inset of Fig. 3a). We define the vortex–antivortex pair correlation function as $G(r) = \langle n_s(0) n_s(r) \rangle$, where $n_s(r) = \sum_\alpha q_\alpha \delta(r - r_\alpha)$ is a signed defect density, $q_\alpha = 1(-1)$ for vortices (antivortices), and r_α is the defect position. The distances are scaled by the average defect separation r_{av}, making $G(r)$ dimensionless. Both the overall domain patterns and the $G(r)$ obtained from the MC simulations (Fig. 3a) reproduce well the results obtained from applying the same analysis to the 2D experimental images (Fig. 3b) of three different hexagonal manganites with different vortex densities: ErMnO$_3$ (0.0046 μm^{-2}), YbMnO$_3$ (0.16 μm^{-2}) and YMnO$_3$ (0.19 μm^{-2}) (see Supplementary Section 3 for details).

In the dual description, the disorder field (that is, vortices and antivortices) condenses on heating across T_c, and this disorder condensation makes the gauge field massive. This Higgs transition
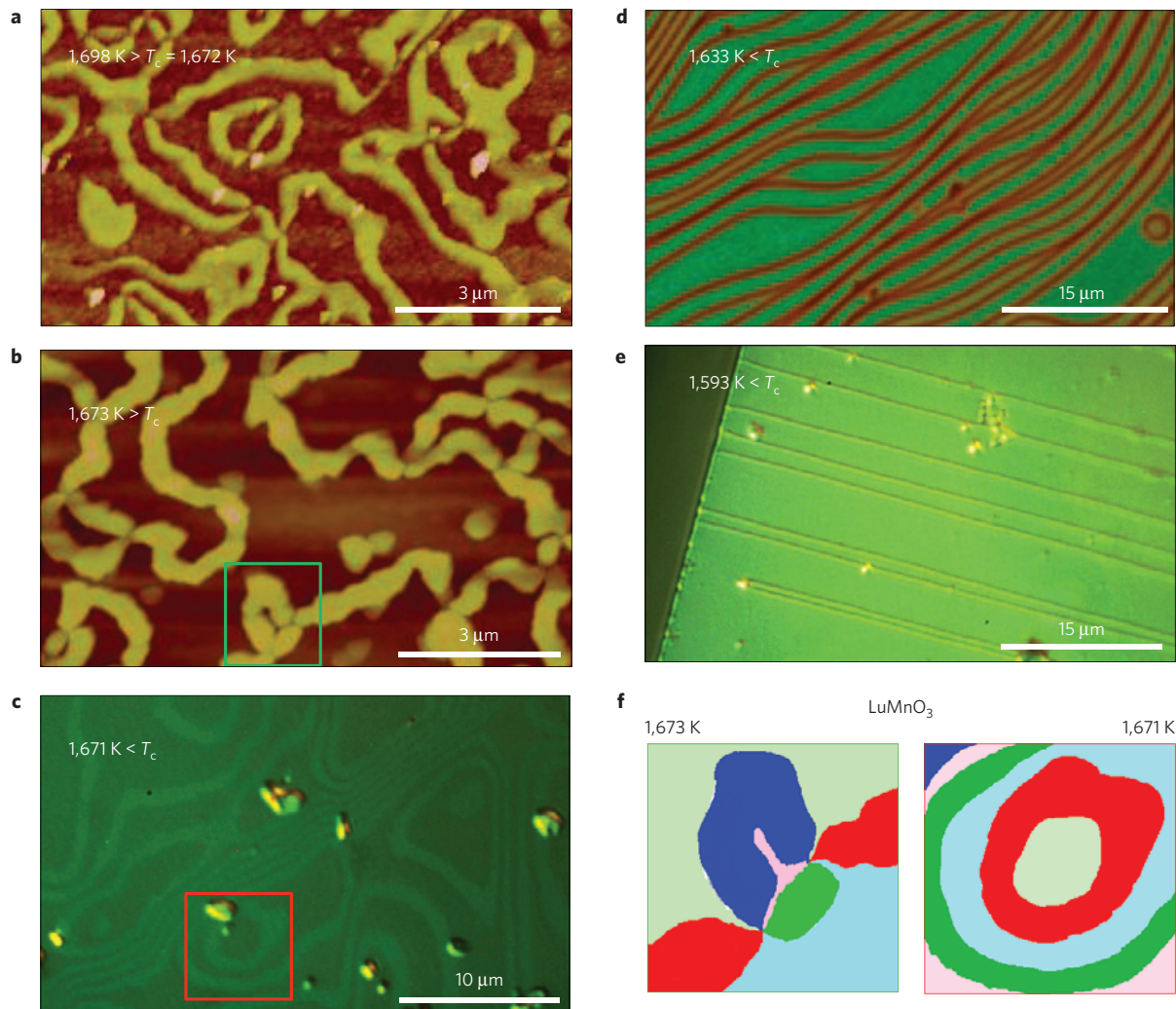
Figure 4 | Domain patterns for different initial annealing temperatures T_i (above, near and below T_c). AFM images (**a**,**b**) and optical images (**c**–**e**) of LuMnO$_3$ ($T_c = 1,672$ K), with T_i indicated in each panel. Adjacent areas of different colours correspond to the domains with the opposite polarizations. Vortices are found only for $T_i > T_c$, whereas stripe and annular domain patterns are observed for $T_i < T_c$. This is illustrated by schematic enlargements in **f**, showing vortices for $T_i = 1,673$ K (1 K above T_c), and annular patterns for $T_i = 1,671$ K (1 K below T_c). The plots in **f** correspond to the data in the green and red boxes in **b**,**c**.

of the vortex field has direct consequences on the non-equilibrium symmetry-breaking process that takes place when the temperature is lowered at a finite rate from an initial temperature T_i close to T_c. Vortices that span the whole system disappear at a much slower rate. Consequently, the final state must be very different, depending on whether the initial temperature T_i is lower or higher than T_c. If $T_i < T_c$, all the vortices form as loops of a finite size (smaller than the system size, with the size distribution set by the Boltzmann factor), implying that they should shrink and disappear on cooling. In contrast, if $T_i > T_c$, a significant ($\sim$70%) fraction of the vortex network comes as an 'infinite string' that spans the whole system[36] and can be expected to survive on cooling. Our experiments and MC simulations confirm this analysis. Figure 4a,b, showing atomic force microscope (AFM) images on LuMnO$_3$ with $T_c = 1,672$ K annealed from 1,698 to 1,673 K, demonstrates the presence of vortices/antivortices, indicating a finite vortex density for $T_i > T_c$. When LuMnO$_3$ is annealed from temperatures lower than T_c, annular domain patterns, high-density wavy stripes, and low-density straight stripes are found with annealing temperatures of 1,671 K, 1,633 K and 1,593 K, respectively. The optical microscope images are shown in Fig. 4c–e. The trend is evident: many vortices

remain in the final state when $T_i > T_c$. In contrast, the final state for $T_i < T_c$ consists of annular patterns or straight stripes, and contains no vortices or antivortices. (Stripes are expected to form owing to the long-range dipolar interactions, which are present in the real system, but are not included in our model.) Indeed, our experimental results and numerical simulations indicate that this discontinuous change in the dynamics of the vortex field can be used to determine T_c in a very precise way ($\pm$1 K/1,672 K = $\pm$0.06%).

Kibble–Zurek mechanism

In the previous section we have seen that the equilibrium properties of RMnO$_3$ ferroelectrics are well described by a Z_6 clock model and that the relevant degrees of freedom freeze below a certain temperature $T < T_c$. This combination provides an ideal setting for testing the KZM. The main difference between the cosmological and laboratory settings is that now the relaxation time and coherence length (and speed of the relevant sound rather than the speed of light) determine the sonic horizon—the linear size $\hat{\xi}$ of regions that can break symmetry in step. The basic idea[18] is to compare the relaxation time τ with the timescale of change of the key parameter (here, relative temperature $\varepsilon = (T - T_c)/T_c$). We assume $\varepsilon(t) = t/\tau_Q$,

where τ_Q is the quench time. The relaxation time $\tau(\varepsilon) = \tau_0/|\varepsilon|^{\nu z}$ (where ν and z are spatial and dynamical critical exponents, and τ_0 is a timescale set by microphysics) determines the reaction time of the order parameter. Relaxation characterized by $\tau(\varepsilon)$ is faster than $|\varepsilon/\dot{\varepsilon}| = t$ outside interval $\hat{t} = (\tau_0\tau_Q^{z\nu})^{1/(1+\nu z)}$ around the transition, so the system can quasi-adiabatically follow the change imposed by the quench. This instant is determined by the equation[18]:

$$\tau(\varepsilon(\hat{t})) = |\varepsilon/\dot{\varepsilon}| = \hat{t}$$

The system will cease to keep up with the imposed change at time $\hat{t}$ before reaching the critical point, while its reflexes are recovered at time $\hat{t}$ (that is, when $\hat{\varepsilon} = (\tau_0/\tau_Q)^{1/(1+\nu z)}$) after the transition. Thus, broken symmetry is chosen by fluctuations when their coherence length is[18]:

$$\hat{\xi} = \frac{\xi_0}{|\hat{\varepsilon}|^\nu} = \xi_0(\tau_Q/\tau_0)^{\nu/(1+\nu z)}$$

The choice of broken symmetry is random within fluctuating domains of this size. Topological defects are then expected to form with the density of one defect fragment per domain. Thus, the scaling of $\hat{\xi}$ with quench rate set by the universality class of the transition translates into the scaling of the defect density. This prediction has been verified for the 3D XY model[37]. Indeed, even the KZM predictions of the actual density (and not just its scaling) are close to these observed[38]. Our experimental results (Supplementary Section 4) for RMnO$_3$, as well as our simulations (see Supplementary Section 2 for the simulation details) of H of equation (1), confirm this prediction and corroborate KZM (Fig. 5). The obtained exponent of $\sim$0.59 is very close to the value $2\nu/(1 + \nu z) \cong 0.57$ that is expected for a 3D XY fixed point: $\nu = 0.67155(27)$ (ref. 39) and $z \cong 2$ (ref. 40). We emphasize that the 3D XY fixed point is a consequence of the Z_6 symmetry of RMnO$_3$ compounds (the Z_6 anisotropy is dangerously irrelevant at $T = T_c$ (refs 34,35)). Moreover, we verify the KZM for rapid quenches (where the authors of ref. 38 observed an unexpected decrease of defect density which they termed 'anti-KZM').

By using the above estimate of one defect fragment per volume of the domain of that linear size, one can estimate the defect density as a function of quench rate and of τ_0 and ξ_0—two dimensionful constants that characterize the system—and its universality class given by the spatial and dynamical critical exponents ν and z.

The essence of the Kibble–Zurek mechanism (KZM) is the randomness of the choices of broken symmetry in domains of size $\hat{\xi}$. This randomness—in addition to defect density—predicts[18] scaling of the winding number W subtended by a contour C. The winding number is the net topological charge: $W = n_+ - n_-$, the difference of the numbers n_+ and n_- of vortices and antivortices inside C. If these charges were assigned at random, the typical net charge would be proportional to the square root of their total number, $n = n_+ + n_-$, inside C, so it would scale as a square root of the area A inside C. Therefore, for contours of a fixed shape, it would scale as the length of the contour, $W \propto \sqrt{A} \propto C$.

According to the KZM, W is set by the winding of the phase along C. In our clock model, broken-symmetry phases correspond to even hours on the clock face. W is then the 'number of days' elapsed along the contour C. As choices of even hours (phases) are random in $\hat{\xi}$-sized domains, the typical net winding number W scales as $\sqrt{C/\hat{\xi}}$–it is proportional to the square root of the number of steps.

This scaling with the square root of the circumference can be tested by finding the net charge of vortices inside C. The results are shown in Fig. 6. The typical winding number (characterized either by the average absolute value $\langle|W|\rangle$ or the dispersion $\sqrt{\langle W^2\rangle}$) indeed scales like $\sqrt{C/\hat{\xi}}$, as long as $C > \hat{\xi}$.
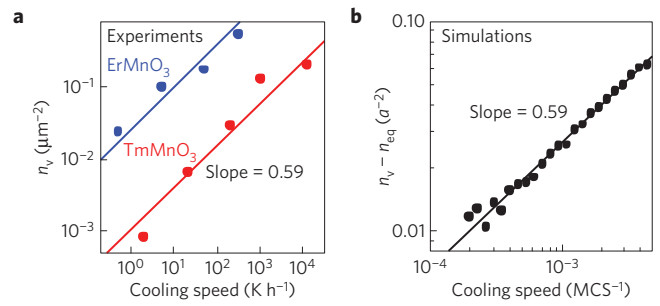
Figure 5 | Dependence of vortex density n_v on cooling rate.
a, Experimental vortex density in the final state as a function of the cooling rate. TmMnO$_3$ ($T_c \approx 1,523$ K) samples with the cooling rates ranging from 2 to 12,000 K h^{-1} and ErMnO$_3$ ($T_c \approx 1,403$ K) samples with the cooling rates ranging from 0.5 to 300 K h^{-1} (ref. 37) were measured. The vortex density as a function of cooling rate is consistent with a power-law dependence with exponent 0.59 (full lines), which is obtained from our MC simulations shown in **b** for a final temperature of 0.92 T_c (black dots), as well as with the prediction of $\sim$0.57 that follows from the Kibble–Zurek mechanism. In **b**, the cooling speed is given in inverse MC sweep (arbitrary units), n_{eq} is the density of the thermally excited vortices subtracted to reveal the KZM scaling (Supplementary Section 2) and a is the lattice parameter.

This scaling dependence changes when the magnitude of W falls below 1. Moreover, the scalings of $\langle|W|\rangle$ and of the dispersion $\sqrt{\langle W^2\rangle}$ diverge in this regime. This may seem surprising, but it is actually predicted by the KZM (ref. 41): $|W| < 1$ occurs when $C < \hat{\xi}$, that is, C normally contains a single defect or none. In this case $\langle|W|\rangle \approx p_+ + p_- = p_{DEFECT}$, while $\sqrt{\langle W^2\rangle} = \sqrt{p_{DEFECT}}$ in terms of probabilities. Moreover, the probability p_{DEFECT} of finding a defect inside C is proportional to the area A subtended by C, accounting for both the change and divergence of the scalings of $\langle|W|\rangle$ and $\sqrt{\langle W^2\rangle}$ seen in Fig. 6a.

Further evidence of the KZM is found in the scaling of $\langle|W|\rangle$ and $\sqrt{\langle W^2\rangle}$ with the deformation of the shape of the contour (and the consequent changes of the area A inside). Figure 6b,c shows that, as long as the size of the contour is large compared to $\hat{\xi}$, the winding number depends only on its length, and not on the area enclosed by the loop. However, as expected, the area becomes important when the number of defects falls below 1 and the scalings of $\langle|W|\rangle$ and $\sqrt{\langle W^2\rangle}$ steepen and diverge.

This prediction can be motivated[41] by using a simple model where defects of opposite charge appear in pairs and both their size and typical separations are given by $\hat{\xi}$. This pairing of vortices and antivortices is an *ad hoc* model, although it can be motivated by considering the 3D geometry of vortex lines and their relation to the vortices that appear as a 2D plane intercepts a 3D sample (see for example, Fig. 2). Moreover, pairing of the oppositely charged defects is obviously consistent[13,42] with the correlation functions seen in Fig. 3.

Conclusions

The observation of the Kibble–Zurek mechanism in a non-equilibrium phase transition with the scaling of defect density determined by the exponents of the 3D XY model provides further confirmation of the emergent U(1) at the critical point of the structural transition. It is then natural to expect a proliferation of vortices right above the transition. However, because the symmetry remains discrete at temperatures away from the critical point, the continuous U(1) vortices that appear in superfluid systems are replaced by the discrete Z_6 vortices observed in hexagonal RMnO$_3$ at room temperature. This novel realization of a 3D XY transition has a unique advantage relative to superfluids: the possibility of freezing vortices in hexagonal RMnO$_3$ provides a
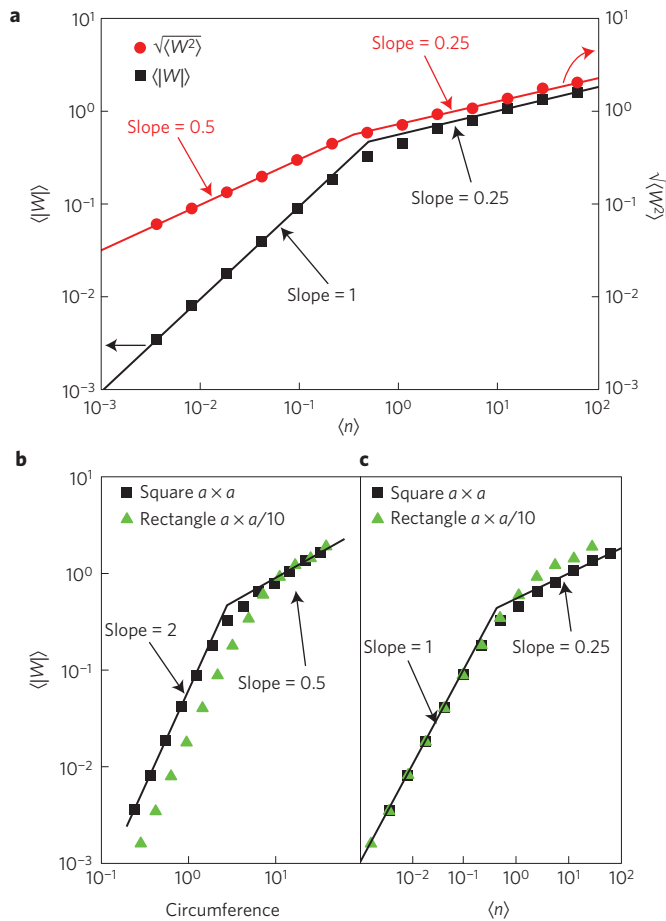
Figure 6 | Winding numbers for KZM defects. Absolute winding numbers $\langle |W| \rangle$ and their dispersions $\sqrt{\langle W^2 \rangle}$ obtained from the coordinates of ~4,100 defects in YMnO$_3$ crystal (Supplementary Section 3), as functions of the average number of defects $\langle n \rangle$ inside the contour C. Typical winding numbers $W = n_+ - n_-$ inside C are predicted by KZM (refs 18,41). Their scaling follows from the key idea that local random choices of broken symmetry in domains of size $\sim\hat{\xi}$ determine defect locations. For contours with circumference $C > \hat{\xi}$, which contain many defects (large average $n = n_+ + n_-$) KZM predicts that $\langle |W| \rangle$ and $\sqrt{\langle W^2 \rangle}$ depend only on C, and vary as $\sqrt{C/\hat{\xi}}$, independently of the shape, area A or average $\langle n \rangle \sim A$ inside C. This may seem surprising, for if defect charges were random, then one would expect winding number (the mismatch between vortices and antivortices inside C) to vary as $\langle n \rangle^{1/2} \sim A^{1/2} \sim C$. **a**, The KZM prediction is confirmed for randomly placed contours of a fixed shape (here squares, like the green one in Fig. 4b). For a fixed shape $C \sim \langle n \rangle^{1/2}$ and large $\langle n \rangle$, typical winding number scaling $|W| \sim \sqrt{C/\hat{\xi}}$ results in $\langle |W| \rangle$ and $\sqrt{\langle W^2 \rangle}$ proportional to $\langle n \rangle^{1/4}$. By contrast, when $\langle n \rangle < 1$, there is usually at most one defect inside C, so W can be only 0, +1, or −1, so $\langle |W| \rangle$ is proportional to the probability p of finding a defect. Moreover, $p \sim A$, so now $\langle |W| \rangle \sim A \sim \langle n \rangle$—typical winding numbers depend on the area A inside C. However, dispersion is proportional to $p^{1/2}$, so $\sqrt{\langle W^2 \rangle} \sim C \sim \langle n \rangle^{1/2}$. Thus, when $\langle n \rangle < 1$, scaling of average $\langle |W| \rangle$ and $\sqrt{\langle W^2 \rangle}$ differ[41]. This is also seen in **a**. **b**, $\langle |W| \rangle$ contours of the same circumference, but with different shapes and, hence, areas that differ by a factor of ~3. As expected, $\langle |W| \rangle$ depends on $C^{1/2}$ for large $\langle n \rangle$, but on $A \sim \langle n \rangle \sim C^2$ for fractional $\langle n \rangle$. **c**, Same data as **b** redrawn as a function of $\langle n \rangle$. In all panels, solid lines show the power laws predicted for $\langle |W| \rangle$ and $\sqrt{\langle W^2 \rangle}$ by KZM (ref. 41). C is normalized so that a square of circumference $C = 4$ ($A = 1$) contains one defect on average. The KZM prediction[18,41] for W, based on randomness of choice of the broken symmetry in domains of size $\sim\hat{\xi}$, is thus verified in all cases.

unique opportunity to study the disorder field (dual theory) and measure the experimental consequences of the Higgs mechanism that arises from its condensation. In particular, geometric properties of the vortex field of RMnO$_3$ can be related to the critical exponents of the dual Abelian gauge theory that describes the disorder field (Box 1). For instance, the critical exponent that controls how the effective line tension of vortices vanishes when T_c is approached from below is $\gamma = \nu_\psi(2 - \eta_\psi)$, where ν_ψ and η_ψ are the critical exponents of the dual or disorder matter field[43]. Because the dual field is described by the same Abelian gauge theory that describes the order parameter field of a charged superfluid, measuring the critical behaviour of vortices in RMnO$_3$ would provide information about the critical exponents of a charged superfluid, such as a strongly type II superconductor.

The implications of our discussion go far beyond multiferroics. For example, experiments[44,45] with rapid cooling of superconducting loops reported that the frequency of trapping a single flux quantum inside scaled with a power which was four times that predicted for large loops. We have seen such steepening in $\langle |W| \rangle \approx p_+ + p_- = p_{\text{DEFECT}}$, which is indeed in the $p_{\text{DEFECT}} < 1$ regime, set by p_{DEFECT}, and thus proportional to $A/\hat{\xi}^2$. Thus, an explanation (based on the fabrication problems) of the apparent divergence between what was thought to be KZM predictions and experiment put forward before turns out to be unnecessary. Instead of the doubling (presumably based on the expected behaviour[46] of $\sqrt{\langle W^2 \rangle}$), the scaling of the frequency of trapping a flux quantum with quench rate quadruples (Fig. 6). Such quadrupling of p_{DEFECT} and $\langle |W| \rangle$, predicted by the KZM (and seen before[44,45]), is hereby confirmed experimentally (Fig. 6).

Last but not least, the confirmation of the KZM in a 3D XY critical point (the same universality class as the λ transition in ^{4}He) suggests that the failure to detect[47] KZM vortices in ^{4}He quench experiments may be due to their rapid annihilation combined with the inability to measure their density right after the quench. Ferroelectrics bypass this problem by immobilizing vortices in the matrix of the material soon after the quench, preventing their annihilation.

References

1. Anderson, P. W. *Basic Notions of Condensed Matter Physics* (Benjamin/Cummings Pub. Co., Advanced Book Program, 1984).
2. Wilson, K. G. The renormalization group: Critical phenomena and the Kondo problem. *Rev. Mod. Phys.* **47**, 773–840 (1975).
3. José, J. V., Kadanoff, L. P., Kirkpatrick, S. & Nelson, D. R. Renormalization, vortices, and symmetry-breaking perturbations in the two-dimensional planar model. *Phys. Rev. B* **16**, 1217–1241 (1977).
4. Onsager, L. The two fluid model for helium II [remarks by L. Onsager on pp. 249–250]. *Nuovo Cimento Suppl.* **6**, 249–250 (1949).
5. Feynman, R. in *Progress in Low Temperature Physics* Vol. I. (ed. Gorter, C.) (North-Holland, 1955).
6. Vilenkin, A. & Shellard, E. P. S. *Cosmic Strings and Other Topological Defects* (Cambridge Univ. Press, 1994).
7. Kibble, T. Phase-transition dynamics in the lab and the universe. *Phys. Today* **60**, 47–52 (September, 2007).
8. Shenoy, S. R. & Chattopadhyay, B. Anisotropic three-dimensional XY model and vortex-loop scaling. *Phys. Rev. B* **51**, 9129–9147 (1995).
9. Domínguez, D., Grønbech-Jensen, N., Bishop, A. R. & Shenoy, S. R. Transformer configuration in three dimensional Josephson lattices at zero magnetic field. *Phys. Rev. Lett.* **75**, 717–720 (1995).
10. Kiometzis, M., Kleinert, H. & Schakel, A. M. J. Critical exponents of the superconducting phase transition. *Phys. Rev. Lett.* **73**, 1975–1977 (1994).
11. Nguyen, A. K. & Sudbø, A. Onsager loop transition and first-order flux-line lattice melting in high-T_c superconductors. *Phys. Rev. B* **57**, 3123–3143 (1998).
12. Ryu, S. & Stroud, D. Nature of the low-field transition in the mixed state of high-temperature superconductors. *Phys. Rev. B* **57**, 14476–14497 (1998).

13. Golubchik, D., Polturak, E. & Koren, G. Evidence for long-range correlations within arrays of spontaneously created magnetic vortices in a Nb thin-film superconductor. *Phys. Rev. Lett.* **104**, 247002 (2010).

14. Kleinert, H. *Gauge Fields in Condensed Matter* (World Scientific Publishing, 1989).

15. Kleinert, H. From Landau's order parameter to modern disorder fields. *Am. Inst. Phys. Conf. Ser.* **1205**, 103–107 (2010).

16. Kiometzis, M., Kleinert, H. & Schakel, A. M. J. Dual description of the superconducting phase transition. *Fortschr. Phys.-Prog. Phys.* **43**, 697–732 (1995).

17. Kibble, T. W. B. Topology of cosmic domains and strings. *J. Phys. A: Math. Gen.* **9**, 1387–1398 (1976).

18. Zurek, W. H. Cosmological experiments in superfluid helium? *Nature* **317**, 505–508 (1985).

19. del Campo, A. & Zurek, W. H. Universality of phase transition dynamics: Topological defects from symmetry breaking. *Int. J. Mod. Phys.* **A 29**, 1430018 (2014).

20. Chuang, I., Durrer, R., Turok, N. & Yurke, B. Cosmology in the laboratory—Defect dynamics in liquid-crystals. *Science* **251**, 1336–1342 (1991).

21. Ruutu, V. M. H. *et al.* Vortex formation in neutron-irradiated superfluid He-3 as an analogue of cosmological defect formation. *Nature* **382**, 334–336 (1996).

22. Bauerle, C., Bunkov, Y. M., Fisher, S. N., Godfrin, H. & Pickett, G. R. Laboratory simulation of cosmic string formation in the early Universe using superfluid He-3. *Nature* **382**, 332–334 (1996).

23. Sadler, L. E., Higbie, J. M., Leslie, S. R., Vengalattore, M. & Stamper-Kurn, D. M. Spontaneous symmetry breaking in a quenched ferromagnetic spinor Bose–Einstein condensate. *Nature* **443**, 312–315 (2006).

24. Weiler, C. N. *et al.* Spontaneous vortices in the formation of Bose–Einstein condensates. *Nature* **455**, 948–951 (2008).

25. Ulm, S. *et al.* Observation of the Kibble–Zurek scaling law for defect formation in ion crystals. *Nature Commun.* **4**, 2290 (2013).

26. Pyka, K. *et al.* Topological defect formation and spontaneous symmetry breaking in ion Coulomb crystals. *Nature Commun.* **4**, 2291 (2013).

27. Lamporesi, G., Donadello, S., Serafini, S., Dalfovo, F. & Ferrari, G. Spontaneous creation of Kibble–Zurek solitons in a Bose–Einstein condensate. *Nature Phys.* **9**, 655–659 (2013).

28. Choi, T. *et al.* Insulating interlocked ferroelectric and structural antiphase domain walls in multiferroic YMnO$_3$. *Nature Mater.* **9**, 253–258 (2010).

29. Mostovoy, M. Multiferroics: A whirlwind of opportunities. *Nature Mater.* **9**, 188–190 (2010).

30. Jungk, T., Hoffmann, A., Fiebig, M. & Soergel, E. Electrostatic topology of ferroelectric domains in YMnO$_3$. *Appl. Phys. Lett.* **97**, 012904 (2010).

31. Lochocki, E. B., Park, S., Lee, N., Cheong, S. W. & Wu, W. D. Piezoresponse force microscopy of domains and walls in multiferroic HoMnO$_3$. *Appl. Phys. Lett.* **99**, 232901 (2011).

32. Chae, S. C. *et al.* Evolution of the domain topology in a ferroelectric. *Phys. Rev. Lett.* **110**, 167601 (2013).

33. Chae, S. C. *et al.* Self-organization, condensation, and annihilation of topological vortices and antivortices in a multiferroic. *Proc. Natl Acad. Sci. USA* **107**, 21366–21370 (2010).

34. Blankschtein, D., Ma, M., Berker, A. N., Grest, G. S. & Soukoulis, C. M. Ordering of a stacked frustrated triangular system in 3 dimensions. *Phys. Rev. B* **29**, 5250–5252 (1984).

35. Oshikawa, M. Ordered phase and scaling in Z(n) models and the three-state antiferromagnetic Potts model in three dimensions. *Phys. Rev. B* **61**, 3430–3434 (2000).

36. Vachaspati, T. & Vilenkin, A. Formation and evolution of cosmic strings. *Phys. Rev. D* **30**, 2036–2045 (1984).

37. Chae, S. C. *et al.* Direct observation of the proliferation of ferroelectric loop domains and vortex–antivortex pairs. *Phys. Rev. Lett.* **108**, 167603 (2012).

38. Griffin, S. M. *et al.* Scaling behavior and beyond equilibrium in the hexagonal manganites. *Phys. Rev. X* **2**, 041022 (2012).

39. Campostrini, M., Hasenbusch, M., Pelissetto, A., Rossi, P. & Vicari, E. Critical behavior of the three-dimensional XY universality class. *Phys. Rev. B* **63**, 214503 (2001).

40. Hohenberg, P. C. & Halperin, B. I. Theory of dynamic critical phenomena. *Rev. Mod. Phys.* **49**, 435–479 (1977).

41. Zurek, W. H. Topological relics of symmetry breaking: Winding numbers and scaling tilts from random vortex–antivortex pairs. *J. Phys. Condens. Matter* **25**, 404209 (2013).

42. Liu, F. & Mazenko, G. F. Defect–defect correlation in the dynamics of 1st-order phase-transition. *Phys. Rev. B* **46**, 5963–5971 (1992).

43. Hove, J. & Sudbo, A. Anomalous scaling dimensions and stable charged fixed point of type-II superconductors. *Phys. Rev. Lett.* **84**, 3426–3429 (2000).

44. Monaco, R., Aaroe, M., Mygind, J., Rivers, R. J. & Koshelets, V. P. Experiments on spontaneous vortex formation in Josephson tunnel junctions. *Phys. Rev. B* **74**, 144513 (2006).

45. Monaco, R., Mygind, J., Rivers, R. J. & Koshelets, V. P. Spontaneous fluxoid formation in superconducting loops. *Phys. Rev. B* **80**, 180501 (2009).

46. Kavoussanaki, E., Monaco, R. & Rivers, R. J. Testing the Kibble–Zurek scenario with annular Josephson tunnel junctions. *Phys. Rev. Lett.* **85**, 3452–3455 (2000).

47. Dodd, M. E., Hendry, P. C., Lawson, N. S., McClintock, P. V. E. & Williams, C. D. H. Nonappearance of vortices in fast mechanical expansions of liquid He-4 through the lambda transition. *Phys. Rev. Lett.* **81**, 3703–3706 (1998).

Acknowledgements

Author contributions

S-W.C. designed and supervised the experiment. W.H.Z. and C.D.B. discussed the simulations and experiments, and wrote the section on the Kibble–Zurek mechanism. X.W. carried out annealing experiments, AFM and PFM work. F.F. performed PFM work. D.F., B.C. and Y.L. analysed vortex–antivortex optical images and V.K. calculated the experimental correlation functions. S-Z.L., Y.K. and G-W.C. simulated the theoretical results. S-Z.L., X.W., S-W.C., W.H.Z., C.D.B. and V.K. co-wrote the paper. All authors discussed the results.

Additional information

Supplementary information is available in the online version of the paper. Reprints and permissions information is available online at www.nature.com/reprints. Correspondence and requests for materials should be addressed to S-W.C.

Competing financial interests